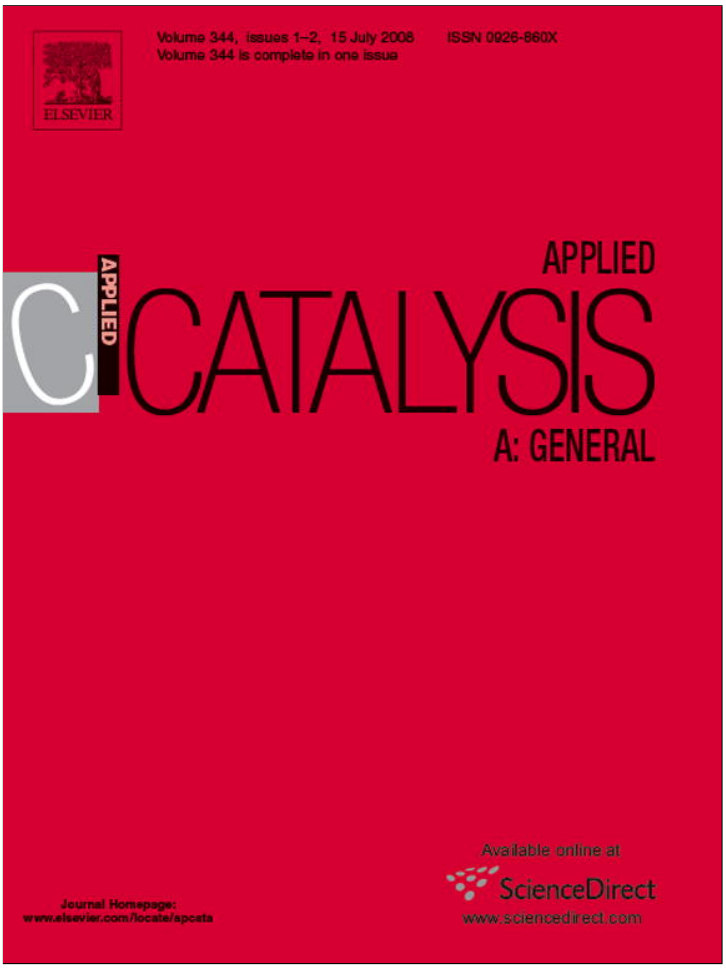

Applied Catalysis A: General 344 (2008) 10–19

Contents lists available at ScienceDirect

Applied Catalysis A: General

journal homepage: www.elsevier.com/locate/apcata

Structural features and performance of $LaNi_{1-x}Rh_xO_3$ system for the dry reforming of methane

M.E. Rivas [a], J.L.G. Fierro [a,*], M.R. Goldwasser [b,**], E. Pietri [b], M.J. Pérez-Zurita [b], A. Griboval-Constant [c], G. Leclercq [c]

[a] Instituto de Catálisis y Petroleoquímica, CSIC, Cantoblanco, 28049 Madrid, Spain
[b] Centro de Catálisis Petróleo y Petroquímica, Escuela de Química, Facultad de Ciencias, Universidad Central de Venezuela, Los Chaguaramos, 40600 Caracas, Venezuela
[c] Unité de Catalyse et Chimie du Solide, UMR CNRS 8181, U.S.T.L., Bâtiment C3, 59655 Villeneuve D'Ascq Cedex, France

ARTICLE INFO

Article history:
Received 8 November 2007
Received in revised form 13 March 2008
Accepted 17 March 2008
Available online 27 March 2008

Keywords:
Nickel catalysts
Ni–Rh perovskite-type precursors
Methane reforming
Catalysts characterization

ABSTRACT

A series of $LaNiO_3$ perovskite-type oxides were synthesized and the influence of the preparation methodology and partial substitution of Ni by Rh on the performance of these solids in the dry reforming of methane was studied. The precursor perovskite-type oxides were synthesized by the citrate sol–gel method and by co-precipitation using K_2CO_3 as precipitating agent. An additional $LaNiO_3$ sample used as reference was prepared by impregnation of La_2O_3 with a nickel nitrate solution. Characterization of the synthesized perovskite-type oxides was followed by X-ray diffraction (*ex situ* and *in situ*), nitrogen adsorption, temperature-programmed reduction and photoelectron spectroscopy. In addition, structural and surface changes produced during reaction were followed by techniques such as thermogravimetric analyses, electron microscopy and photoelectron spectroscopy. Highly homogeneous and crystalline oxides were obtained with various particle sizes depending on the synthesis method. Results show influence of the synthesis procedure on the catalytic performance of these solids by formation of different lanthanum phases during reaction. It is observed that at low reaction temperatures (400–500 °C), all samples presented similar activity while at higher temperatures (550–600 °C) the solid prepared by impregnation was more active. Partial substitution of nickel by rhodium (5% mol) produces an increase in the catalytic activity. No deactivation of all synthesized solids was observed after 24 h on-stream.

1. Introduction

Methane reforming reactions are currently used to produce synthesis gas and/or hydrogen. Due to the increase on H_2 demand and the importance of synthesis gas for further reactions, the role of methane reforming catalysts have recently become more important. Among these reactions, the carbon dioxide reforming of methane (dry reforming) is of great interest since it allows production of H_2/CO ratios suitable for the synthesis of a wide variety of valuable hydrocarbons and oxygenates [1–3]. However, since the dry reforming is a highly endothermic reaction, Eq. (1), it has to be performed at high temperature and low pressure to achieve maximum conversions.

$$CH_4 + CO_2 \rightarrow 2\,CO + 2\,H_2, \qquad \Delta H^\circ = +59.1\,\text{kcal/mol} \tag{1}$$

It is well known that nickel [4,5] and noble metals [4–6] are active catalysts for the dry reforming of methane. In addition perovskite-type oxides [7,8] and transition metal carbides (especially Mo) have been considered for CO_2 reforming [9–11] although under reaction conditions the later systems are only stable at high pressure.

The major disadvantage of the dry reforming reaction is catalyst deactivation caused by coke formation on the active surface and by structural transformations, sintering and recombination of the active components caused by the high operation temperatures needed in this process (~800 °C).

Carbon deposits are developed on the surface of metal particles mainly through two reactions: methane decomposition and Boudouard's reaction in the following equations.

$$CH_4 \rightarrow C + 2\,H_2, \qquad \Delta H_{298} = +17.9\,\text{kcal/mol} \tag{2}$$

$$2\,CO \rightarrow CO_2 + C, \qquad \Delta H_{298} = -41.2\,\text{kcal/mol} \tag{3}$$

Ni catalysts are of special interest since they present a high initial activity for this reaction, interesting redox properties and relatively low cost. However, it is difficult to prevent sintering of

* Corresponding author.
** Corresponding author. Tel.: +58 212 7812349; fax: +58 212 2392162.
E-mail addresses: jlgfierro@icp.csic.es (J.L.G. Fierro), mgoldwas@reacciun.ve (M.R. Goldwasser).

0926-860X/$ – see front matter © 2008 Published by Elsevier B.V.
doi:10.1016/j.apcata.2008.03.023

nickel and carbon deposits at high temperatures [12–14]. Even noble metals such as Ru, Rh, Pt and Ir are known to be less coke forming under reaction [15,16].

Similarly, it has been reported that incorporation of alkali, alkaline-earth and lanthanide oxides and the use of highly dispersed metal particles on a substrate contribute to reduce carbon deposition and hence to increase catalytic stability [17,18].

A particularly attractive option for this purpose is the use of catalysts derived from perovskite-type oxides precursors which fulfill requirements of metal dispersion and thermal stability. Many studies have been carried out with the aim to synthesize mixed-oxides with perovskite-type structure [8,19–21] suitable for methane conversion, such as steam reforming, partial oxidation and dry reforming. Perovskite-type oxides of general formula ABO_3 (A: alkaline earth or lanthanide; B: transition element) in which A is a large cation, responsible for the thermal resistance, and B is a redox cation responsible for catalytic activity are highly stable under the severe conditions imposed by these reactions such as high temperature and presence of steam in the reaction atmosphere. When subjected to reduction processes, perovskite-type oxides produce very small particles, in the order of the nanometers, with high metallic dispersion [7,8]. The efficient use of these catalyst precursors necessarily implies a high dispersion of metal phase which can be achieved by controlled segregation of the active phase.

Thus, it is expected that $LaNiO_3$-based catalyst precursors will satisfy not only the stability requirements but also produce highly dispersed Ni metal particles upon reduction. In addition, partial substitution of Ni by a second metal will inhibit coke formation. Rh seems to be the metal that better fulfils this requirement with certain compromise between activity and stability [15,16].

It is also well established that the synthesis methodology plays an important role in the catalytic performance of methane reforming catalysts. The different synthesis methods used generate structural, surface and textural changes in the properties of the materials influencing their catalytic behavior [22].

The present contribution describes the influence of the synthesis method (co-precipitation, sol–gel, and impregnation) and of the partial substitution of nickel by rhodium on the surface and catalytic properties in the dry reforming of methane of catalysts obtained from lanthanum nickel-based perovskite-type oxides precursors.

2. Experimental

2.1. Catalyst precursors preparation

The $LaNiO_3$ and $LaNi_{0.95}Rh_{0.05}O_3$ perovskite-type oxides precursors were synthesized according to the modified citrate [23] and by co-precipitation [24] methods. They are referred, according to the synthesis method used, as $LaNi_{0.95}Rh_{0.05}O_3$-sg and $LaNiO_3$-sg when synthesized by sol–gel, $LaNi_{0.95}Rh_{0.05}O_3$-cp and $LaNiO_3$-cp synthesized by co-precipitation and $LaNiO_3$-imp synthesized by impregnation.

2.1.1. Sol–gel

Stoichiometric amounts of $La(NO_3)_3{\cdot}xH_2O$, $Ni(NO_3)_3{\cdot}6H_2O$ and $RhCl_3{\cdot}xH_2O$ (Merck, reagent grade) were dissolved in distilled water and added to a second solution containing equimolecular amounts of citric acid (99.5%, Riedel-de Haën) and ethylene glycol (99.5%, Riedel-de Haën) as a polydentate ligand. The excess water was slowly removed in a rotary-evaporator until a viscous liquid was obtained. Subsequently, it was slowly heated in air (1 °C/min from room temperature up to 750 °C) and kept at this temperature for 5 h. These conditions are essential to obtain a crystalline material.

2.1.2. Co-precipitation

$LaNiO_3$ and $LaNi_{0.95}Rh_{0.05}O_3$ were synthesized by simultaneous precipitation of nickel and lanthanum ions from a solution of their nitrate salts and $RhCl_3{\cdot}xH_2O$ with K_2CO_3 as precipitating agent. The salts $La(NO_3)_3{\cdot}xH_2O$ (Merck, reagent grade), $RhCl_3{\cdot}xH_2O$ and $Ni(NO_3)_3{\cdot}6H_2O$ (Merck, reagent grade) were dissolved in distilled water to obtain 1 M solutions. Both solutions were mixed together under vigorous stirring. Then, a stoichiometric amount (plus 10% excess) of an aqueous solution of K_2CO_3 (99.0% minimum, Johnson Matthey) was rapidly added. Under basic conditions (pH > 9), water was partially evaporated by heating the solution at ~70 °C. The precipitate was then washed with ice-cooled distilled water until neutral pH of the filtrate, dried at 100 °C for 4 h and calcined at 750 °C for 5 h.

A reference $LaNiO_3$ was synthesized by impregnation of a previously calcined La_2O_3 with an aqueous solution of nickel nitrate. The excess of water was slowly removed in a rotary-evaporator and the solid was calcined at 500 °C for 5 h, in order to avoid formation of a La–Ni spinel phase.

2.2. Catalysts characterization

The solids were characterized before and after catalytic tests by means of different techniques such as *in situ*, *ex situ* X-ray diffraction (XRD), specific surface area (BET), temperature-programmed reduction and oxidation (TPR, TPO), thermogravimetric analysis (TGA) and photoelectron spectroscopy (XPS).

X-ray powder diffraction (XRD) experiments were conducted using a Seifert 3000P instrument with nickel-filtered Cu Kα radiation (λ = 0.1538 nm). The diffractograms were collected in the 5–80° (2θ) range at 2°/min. *In situ* X-ray diffraction experiments were performed using a Siemens D-8 advanced instrument with a Cu Kα radiation source (λ = 0.1538 nm) for crystalline phase detection between 10° and 80° (2θ) and under temperature-programmed reduction (TPR) in 3% H_2/N_2 (50 ml/min) at a rate of 10 °C/min from room temperature to 800 °C, keeping this temperature for 2 h. Phase identification was carried out by comparison with JCPDF standard spectra software. Nickel crystallites particle size were determined by means of the Scherrer' equation using the Ni (1 1 1) reflection at 2θ = 44.5° for line broadening measurements. Specific surface areas were calculated using the BET equation from nitrogen adsorption isotherms, recorded at the temperature of liquid nitrogen on a Micromeritics ASAP 2100 apparatus. In order to get more accurate results, adjustment were performed at low pressures using multi-point's determinations. Prior to the adsorption measurements, samples were out gassed at 250 °C.

Temperature-programmed reduction experiments were carried out on a semiautomatic Micromeritics TPD/TPR 2900 apparatus interfaced with a microcomputer. Samples of about 20 mg were placed in a U-shaped quartz tube purged in a synthetic air stream (150 °C, 1 h) and then cooled to room temperature. Reduction profiles were then recorded by passing a 10% H_2/Ar flow at 50 ml/min while heating at a rate of 10 °C/min from room temperature to 800 °C. A cold-trap was placed just before the TCD of the instrument to remove the water from the exit stream.

The amount of coke deposited on the used catalysts was determined by thermogravimetric analysis (TGA/SDTA 851^e Mettler Toledo) measuring the weight change of the coked catalysts brought about during oxidation at high temperature. The analysis was carried out by increasing sample temperature from 25 to 900 °C (5 °C/min, 20% O_2/N_2 mixture).

Surface analyses were performed on a VG Escalab 200R electron spectrometer provided with Al Kα X-ray source ($h\nu$ = 1486.6 eV, 1 eV = 1.6302×10^{-19} J) and a hemi-spherical electron analyzer. The powder samples pressed in 8-mm diameter copper troughs

were fixed on the XYZ manipulator. The base pressure in the analysis chamber was kept below 4×10^{-9} mbar during data acquisition. The pass energy of the analyzer was set at 50 eV, for which the resolution as measured by the full width at half maximum (FWHM) of the Au $4f_{7/2}$ core level was 1.7 eV. The binding energies were referenced to C1s peak at 284.6 eV due to adventitious carbon. Data processing was performed with a XPS peak program, spectra were decomposed with a least squares fitting routine provided with the software with Gaussian/Lorentzian (90/10) product function and after subtracting a Shirley background. Atomic fractions were calculated using peak areas normalized on the basis of sensitivity factors.

2.3. Transmission electron microscopy

TEM images for used catalysts were recorded with a JEOL 2000 FX microscope, working with an acceleration voltage of 200 kV. Specimens for TEM were prepared by ultrasonically dispersing some powder sample in iso-octane and placing a droplet of the suspension on a copper grid covered with a carbon film.

2.4. Catalytic activity

Activity measurements were carried out in a continuous flow fixed-bed catalytic reactor working at atmospheric pressure. 60 mg catalyst was placed between quartz glass plugs in the centre of a cylindrical tube reactor (12 mm i.d.). Internal and external temperatures of the catalyst reactor were measured by Ni–Cr thermocouples.

Prior to activity measurements, catalyst precursors were reduced in a 10% H_2/N_2 mixture at 700 °C for 2 h to generate the metal phase (Ni^0 or Ni^0–Rh^0). Subsequently, the reactor was flushed in nitrogen flow while cooling to room temperature. The reaction was carried out by feeding a $CH_4/CO_2 = 1$, 80% N_2 as a diluent at a total flow of 140 ml/min, WHSV = 140 h^{-1} and scanning reaction temperatures between 400 and 650 °C. Stability tests were performed at 550 °C for 24 h. Reaction products were on-line analyzed by a Varian 3400 gas-chromatograph provided with thermal conductivity detector and columns packed with Porapak N and 13X molecular sieves. Estimated error of gas-phase composition was within 5%.

3. Results and discussion

3.1. Crystalline structure

Fig. 1 shows the X-ray diffraction patterns of perovskite-type oxide $LaNi_{1-x}Rh_xO_3$ ($x = 0$, 0.05) synthesized by sol–gel and co-precipitation methods. In all cases the main diffraction peaks appeared at 32.8°, 47.0° and 58.0°, characteristic of $LaNiO_3$ rhombohedra structure (JCPDF 33–0711) [19,25]. It is interesting to notice that samples prepared by co-precipitation are more crystalline than those obtained by sol–gel as it can be seen by the intensities of XRD patterns. Similar results have been reported by Norman and Morris [22]. The authors attributed the result to the fact that the co-precipitation method promotes an "intimate" mixture of the precursors. This in turn results in a lower decomposition temperature of the Ni precipitate through a concerted decomposition reaction during the synthesis process. This fact would lead to more crystalline materials. In addition, our results showed the presence of peaks of a minor NiO phase due to segregation of a very small fraction of nickel to the surface. No changes in the diffraction pattern of perovskite-type oxide or crystalline Rh_2O_3 phase formation were observed in $LaNi_{0.95}Rh_{0.05}O_3$ samples.

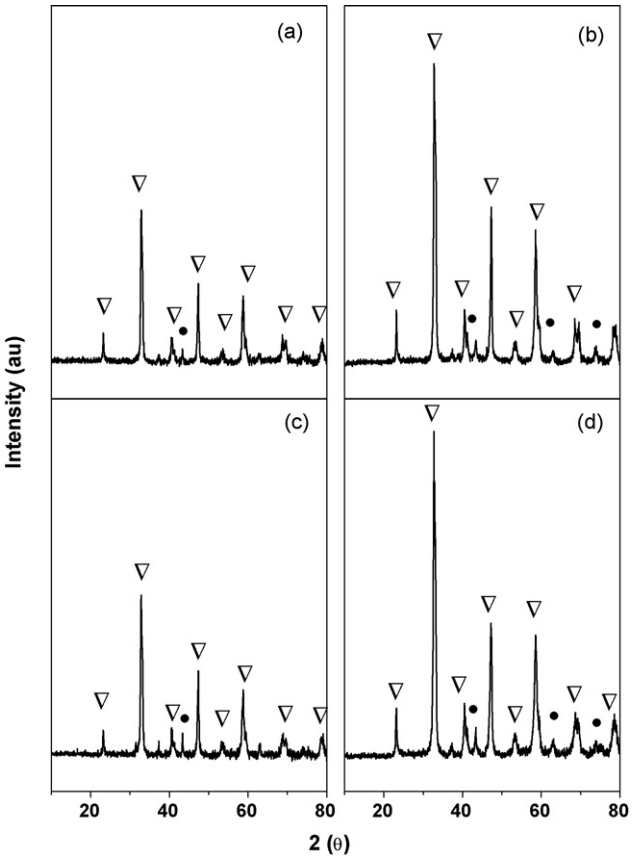

Fig. 1. X-ray diffraction profiles of perovskites: (a) $LaNiO_3$-sg; (b) $LaNiO_3$-cp; (c) $LaNi_{0.95}Rh_{0.05}O_3$-sg; (d) $LaNi_{0.95}Rh_{0.05}O_3$-cp; (▽) $LaNiO_3$; (●) NiO.

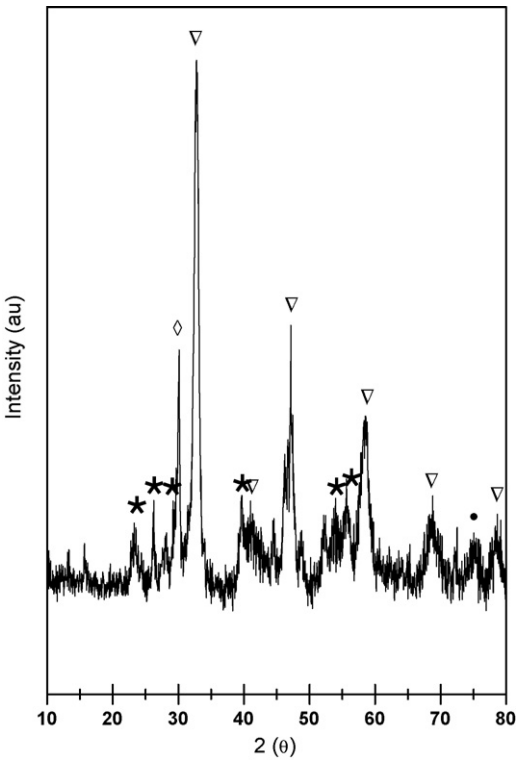

Fig. 2. X-ray diffraction profiles of $LaNiO_3$-imp: (▽) $LaNiO_3$; (●) NiO; (*) La_2O_3.

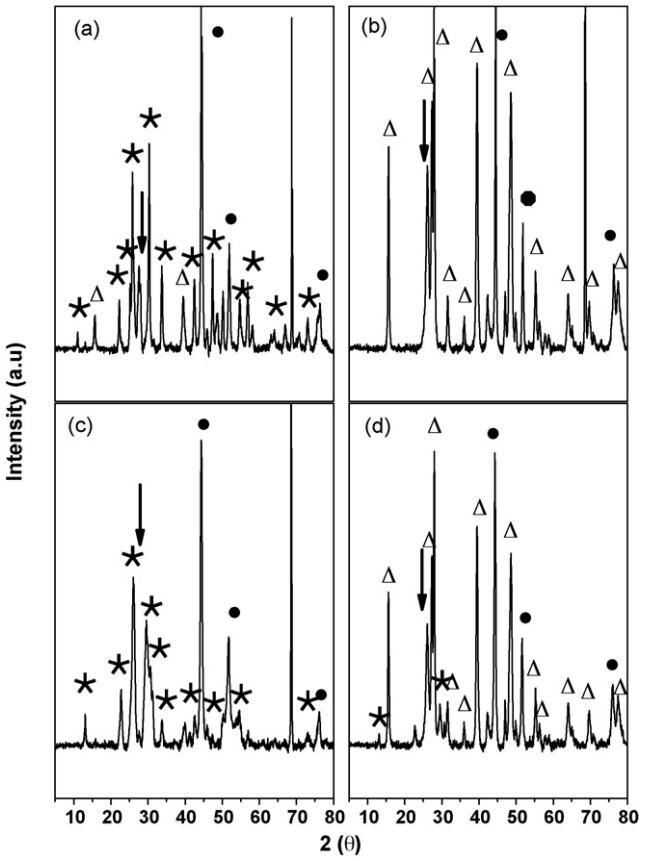

Fig. 3. X-ray diffraction profiles of the catalysts after on-stream operation: (a) $LaNiO_3$-sg; (b) $LaNiO_3$-cp; (c) $LaNi_{0.95}Rh_{0.05}O_3$-sg; (d) $LaNi_{0.95}Rh_{0.05}O_3$-cp; (●) Ni^0; (*) $La_2O_2CO_3$; (△) $La(OH)_3$; (↓) C.

Fig. 2 shows the diffraction pattern of the perovskite-type oxide precursor synthesized by impregnation. As can be observed, the pattern exhibits the characteristic diffraction peaks of $LaNiO_3$ structure, assessing that a solid-state reaction between NiO particles deposited on the surface and the upper layers of La_2O_3 occurs during air calcinations yielding the $LaNiO_3$ perovskite-type structure.

Characterization of the after reaction catalysts used in the dry reforming of methane shows that the structure was completely different from that of their calcined counterparts (Fig. 3). XRD patterns showed one peak at 44.4°, indexed to Ni^0 (JCDF 0031043) and peaks indexed to $La(OH)_3$ and $La_2O_2CO_3$ species. This lanthanum dioxomonocarbonate phase has been claimed as responsible for removal of carbonaceous deposits developed at its interface with the Ni^0-crystallites [8,26,27].

When subjected to reaction conditions, Ni^0 particle size increased as compared to that of Ni^0 in the reduced samples, except for that obtained from the $LaNiO_3$-sg precursor (Table 1). The observed increase in Ni^0 crystallite size was more marked for catalysts derived from co-precipitated precursors than for those synthesized by the sol–gel method. Accordingly with these changes, lanthanum phases present in used samples were found to depend on the synthesis method (see Table 1). Thus, co-precipitated samples displayed intense peaks of $La(OH)_3$ (JCPDF 036-1481) and less intense of $La_2O_2CO_3$ phase (JCPDF 01-084-1963) whereas the opposite occurred in sol–gel samples. In addition, peaks of graphitic carbon were found in all used samples with their intensity following an opposite trend to that of the $La_2O_2CO_3$ phase, suggesting that this La-dioxomonocarbonate species contributes to the gasification of carbonaceous deposits.

3.2. Specific surface area

Table 1 compiles the BET specific surface area of air-calcined precursors (750 °C, 5 h). The observed values (3–5 m^2/g) are rather low and similar to those previously reported for perovskite-type oxides calcined at 700–900 °C. In agreement with previous work [16], the specific surface area of high temperature calcined perovskite-type oxides, mainly corresponds to the external area of particles approaching a spherical geometry, characteristic of non-porous materials. For the catalyst prepared by impregnating of La_2O_3 with nickel salt and used as reference, the obtained surface area is 10 m^2/g. This higher surface area could be attributed to the lower calcined temperature used (500 °C). Upon calcination at 750 °C, the surface area of $LaNiO_3$-imp tends to approach the values observed for other $LaNi_{1-x}Rh_xO_3$ ($x = 0$, 0.05) samples. However, at this higher temperature a La–Ni spinel is detected at the surface of the catalysts. Those changes in specific areas are related to the grain and crystal sizes: the larger the grain and crystal sizes, the smaller the specific surface area [28].

3.3. Reduction characteristics of precursor catalyst

3.3.1. In situ X-ray diffraction analyses

Reducibility and stability studies of $LaNi_{1-x}Rh_xO_3$ ($x = 0$, 0.05) perovskite-type oxides were carried out by means of TPR and *in situ* XRD analyses. Fig. 4 shows diffraction patterns of $LaNiO_3$-sg oxide precursor exposed to a reducing media. It is observed that upon increasing reduction temperature, Ni^{3+} cations reduce to Ni^0 whereas lanthanum converts to La_2O_3. All diffraction patterns show a phase change at ~400 °C, attributed to the reduction of the $LaNiO_3$ phase into a brownmillerite intermediate structure $La_2Ni_2O_5$ [19]. At temperatures above 600 °C the crystal structure collapses with the subsequent formation of Ni^0 crystallites deposited on the La_2O_3. These results are in agreement with previously reported observations [29].

By applying the Scherrer's equation to the most intense diffraction peaks in the XRD patterns [30] the average crystallite size values of the calcined and reduced samples were calculated. For the calcined samples, the most intense peak of the perovskite-type phase at 32.8° was selected, while it was chosen as 44.5° for the reduced samples. Main crystalline phases and the average crystallite sizes are shown in Table 1. As observed, crystallite sizes

Table 1
X-ray diffraction analysis, mean particle size and BET specific surface area of perovskite-type oxide precursors

Catalyst precursors	Main phases (calcined)	Mean particle size (calcined) (nm)	Main phases (reduced)	Mean particle size (reduced) (nm)	Main phases (after test)	Mean particle size (after test) (nm)	Specific surface ($m^2/g \pm 2\%$)
$LaNiO_3$-sg	$LaNiO_3$	22	Ni^0, La_2O_3	21	$La_2O_2CO_3$, $La(OH)_3$, Ni^0, C	22	3
$LaNiO_3$-cp	$LaNiO_3$	16	Ni^0, La_2O_3	15	$La(OH)_3$, $La_2O_2CO_3$, La_2O_3, Ni^0, C	38	7
$LaNi_{0.95}Rh_{0.05}O_3$-sg	$LaNiO_3$	16	Ni^0, La_2O_3	17	$La(OH)_3$, $La_2O_2CO_3$, Ni^0, C	29	4
$LaNi_{0.95}Rh_{0.05}O_3$-cp	$LaNiO_3$	15	Ni^0, La_2O_3	13	$La(OH)_3$, $La_2O_2CO_3$, La_2O_3, Ni^0, C	38	8
$LaNiO_3$-imp	$LaNiO_3$	13	Ni^0, La_2O_3	56	–	–	10

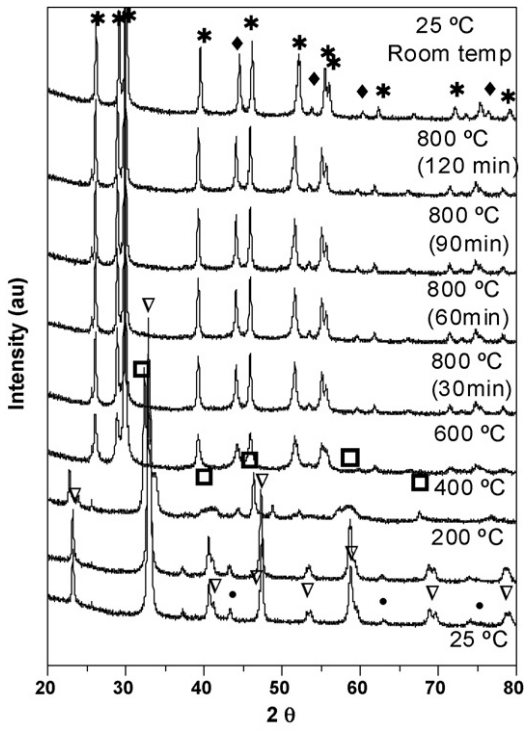

Fig. 4. *In situ* XRD of $LaNiO_3$-sg as synthesized and reduced at different temperatures: (▽) $LaNiO_3$; (●) NiO; (*) La_2O_3; (◆) Ni^0; (□) $La_2Ni_2O_5$.

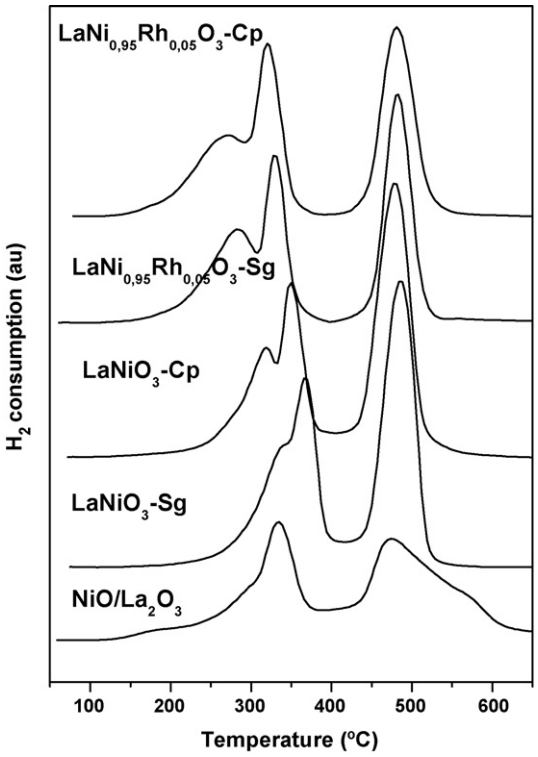

Fig. 5. Temperature-programmed reduction profiles of oxide precursors.

of calcined samples are in the order of 15–22 nm, being somewhat larger for $LaNiO_3$-sg. Similarly, crystallite sizes of Ni^0 in the H_2-reduced samples showed the same trend than the calcined perovskite-type counterparts, indicating that no sintering of metal particles occurred during H_2-reduction.

3.3.2. Temperature-programmed reduction (TPR) of precursor oxides and oxidation (TPO) of used catalyst

Since the active phase of $LaNi_{1-x}Rh_xO_3$ catalysts in the reforming reaction is the metal (Ni^0/Rh^0), activation of the oxide precursors in a reducing atmosphere was performed prior to reaction and followed by TPR analysis. Fig. 5 displays the TPR profiles for all $LaNi_{1-x}Rh_xO_3$ samples. Two major H_2-consumption peaks were observed: one at around 490–500 °C (peak c) and another at lower temperatures, which show maxima in the range 300–320 °C for the samples with rhodium (peak b) and at 340–360 °C for the samples without rhodium. A third smaller broad H_2 component (peak a) overlapping with peak b and extending in the range 270–310 °C was also observed. In agreement with *in situ* XRD data, peak b could be assigned to reduction of Ni^{3+} to Ni^{2+} with concomitant formation of $La_2Ni_2O_5$, while peak c at higher temperature is associated with reduction of Ni^{2+} ions in the brownmillerite phase to Ni^0 and La_2O_3, in agreement with X-ray diffraction data (see below). The resulting Ni^0 metal particles, which are the active phase in the dry methane reforming reaction, remain highly dispersed on the lanthanum oxide phase (Ni^0/La_2O_3). If $LaNiO_3$ is the only phase present in this sample the intensity ratio of the second to the first peak should be 2; however, the observed 1.8 value suggests that a small amount of a separate NiO phase is also present (NiO → Ni^0).

Interestingly, TPR profile of impregnated NiO/La_2O_3 sample is quite similar to those of $LaNi_{1-x}Rh_xO_3$ perovskite-type oxides although main peaks (peaks b and c) are shifted by ~40 °C toward lower temperatures. It may also be observed that the high temperature peak is broader for this sample than for the perovskite-type ones. This is probably due to the combined reduction of the intermediate phase $La_2Ni_2O_5$ and of NiO particles with higher interaction with the support. Similar results have been reported by Requies et al. [31] on the reduction of perovskite-type oxides generated by solid-sate reaction of NiO with La_2O_3. This behavior is attributed to the higher surface area shown by the impregnated Ni/La_2O_3 sample. Since the rate of reduction is proportional to the number of exposed Ni^{2+}/Ni^{3+} species per unit weight, a higher reduction rate is expected for the impregnated sample. In addition, since the reduction process of a metal oxide is controlled by diffusion of water molecules generated in the sub-surface layers across the metallic shell, reduction of smaller $LaNiO_3$ particles (higher area) is expected to be enhanced.

The reduction profiles of the two $LaNi_{0.95}Rh_{0.05}O_3$ samples were similar to that of $LaNiO_3$ precursors although peaks a and b appear shifted by ~20 °C toward lower temperatures. Since Rh^{3+} reduces to Rh^0 at lower temperatures than Ni^{3+} and Ni^{2+}, it is expected that the generated Rh^0 crystallites favor the reducibility of nickel cations via spillover of H-atoms from Rh crystallites [32]. It can be noticed that the position of peak c does not change with the addition of Rh. Since peak c can be associated to the reduction of Ni^{2+} ions in the brownmillerite phase, the promotion effect of Rh is probably camouflaged by diffusion effects, such as slow water removal. On the other hand, the presence of Rh has a more marked effect on the reduction of NiO segregated from the perovskite-type structure (peaks a and b).

For the after reaction samples, the amount of carbon deposited on the used catalysts during the stability test was determined by temperature-programmed oxidation. The profiles (Fig. 6A) clearly show a carbon combustion step for all catalysts. However, due to the oxidation of the metallic active sites (weight increase) overlapping with oxidation of carbon deposits (weight loss); it was difficult to obtain reliable quantification of the deposited carbon by this technique.

Two types of carbon deposits on the catalysts from $LaNiO_3$-cp and $LaNi_{0.95}Rh_{0.05}O_3$-cp precursors were observed by DTA (Fig. 6B).

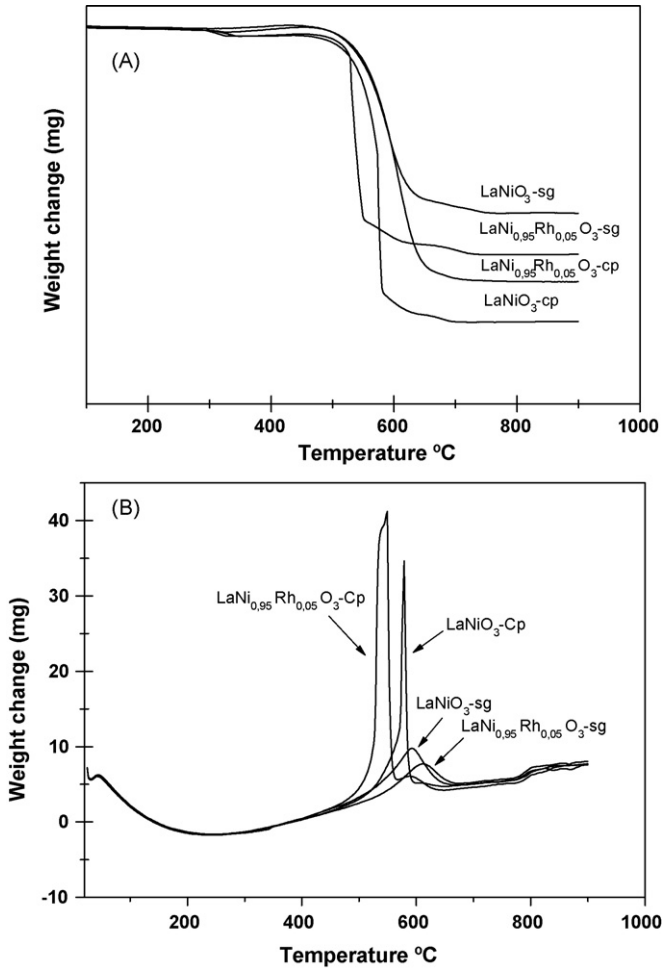

Fig. 6. (A) Temperature-programmed oxidation curves of the catalysts after the stability test. (B) DTA profiles for the used catalysts.

The strong exothermic peak at 549 (shoulder at 593 °C) and 578 °C (shoulder at 611 °C) is related to oxidation of graphitic-like carbon and filamentous carbon, respectively [33]. However, an exothermic peak at 593 °C for $LaNiO_3$-sg and 611 °C for $LaNi_{0.95}Rh_{0.05}O_3$-sg is associated to oxidation of graphitic-like filaments.

3.4. Surface composition

The chemical state of the elements and surface composition of calcined $LaNi_{1-x}Rh_xO_3$ perovskite-type oxides, were revealed by X-ray photoelectron spectroscopy. Table 2 summarizes the binding energies of O 1s, C 1s, Ni $2p_{1/2}$, La $3d_{5/2}$ and Rh $3d_{5/2}$ core-levels of calcined $LaNi_{1-x}Rh_xO_3$. Due to overlapping of Ni $2p_{3/2}$ and La $3d_{3/2}$ signals, the determination of the less intense Ni $2p_{1/2}$ component of the Ni 2p doublet was selected for binding energy measurements and quantification. The Ni $2p_{1/2}$ binding energies at 872.9–873.1 eV (Table 2) point to the presence of ionic nickel species. The corresponding binding energies of La $3d_{5/2}$ peak at 834.5–834.7 eV (Table 2) are lower than those measured for $La(OH)_3$ and similar to that of La_2O_3 [34]. The low resolution of the two La $3d_{5/2}$ peak components, suggests the presence of other species such as $La_2O_2CO_3$ and/or $La(OH)_3$ [35].

The chemical state of oxygen on the surface was also examined. O 1s spectra of all samples, shown in Fig. 7, exhibited three components at: (i) 528.4–528.9 eV; (ii) 530.2–530.9 eV; (iii) 531.5–532.4 eV. Type (i) peak is usually ascribed to weakly bonded oxygen (O^{2-}), while types (ii) and (iii) components may arise from lattice oxygen and hydroxyl/carbonate groups, respectively [36,37]. C 1s core-level showed two components at 284.9 and 285.6 eV due to CC/CH and C–O bonds, respectively, of carbon contamination, and a third one at 289.2–289.4 eV which is

Table 2
Binding energy (eV) of core electrons of LaNi perovskite-type oxides

Calcined Samples	La $3d_{5/2}$	Ni $2p_{1/2}$	C 1s	O 1s	Rh $3d_{5/2}$
$LaNiO_3$-sg	834.7	873.0	289.4	529.0 (33) 530.7 (39) 532.1 (28)	–
$LaNiO_3$-cp	834.6	873.1	289.2	528.9 (34) 530.7 (34) 532.0 (32)	–
$LaNi_{0.95}Rh_{0.05}O_3$-sg	834.6	873.1	289.4	529.1 (34) 530.9 (37) 532.0 (29)	309.4
$LaNi_{0.95}Rh_{0.05}O_3$-cp	834.5	872.9	289.3	529.0 (38) 530.7 (37) 532.0 (25)	309.4

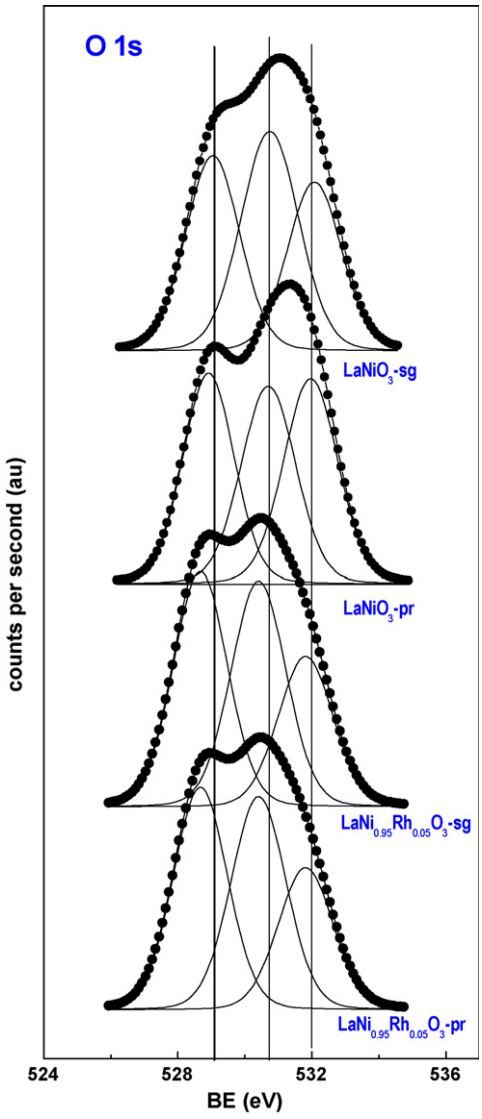

Fig. 7. Phoelectron spectra of the O 1s core-level of oxide precursors: $LaNiO_3$-sg, $LaNiO_3$-cp, $LaNi_{0.95}Rh_{0.05}O_3$-sg, and $LaNi_{0.95}Rh_{0.05}O_3$-cp.

Table 3
Surface atomic ratios of calcined LaNi perovskite-type oxides

Samples	Ni/La (at)	Rh/La (at.)	CO_3^{2-}/La (at.)
$LaNiO_3$-sg	1.295	–	0.701
$LaNiO_3$-cp	1.140	–	0.782
$LaNi_{0.95}Rh_{0.05}O_3$-sg	0.904	0.101	0.604
$LaNi_{0.95}Rh_{0.05}O_3$-cp	1.116	0.106	0.576

characteristic of carbonate species [36,37]. These carbonate structures are developed in La-based perovskite-type oxides as a consequence of carbonation of the basic La^{3+} cations when exposure to room atmosphere. For the two $LaNi_{0.95}Rh_{0.05}O_3$ samples, the binding energy of Rh $3d_{5/2}$ signal appeared at 308.8–309.2 eV, which is typical of Rh^{3+} ions surrounded by oxide anions [38].

Quantification of Ni/La and Rh/La surface atomic ratios are summarized in Table 3, calculated from the intensities of La $3d_{5/2}$, Ni $2p_{1/2}$ and Rh $3d_{5/2}$ signals with atomic sensitivity factors given by Wagner et al. [39]. It can be noted that the Ni/La ratios are slightly higher than the expected theoretical values derived from sample composition for both $LaNiO_3$ and $LaNi_{0.95}Rh_{0.05}O_3$ samples. The Ni-enrichment observed in $LaNiO_3$ samples agrees with TPR profiles which showed the presence of a minor, separate NiO phase deposited on the $LaNiO_3$ substrate. In addition, surface La^{3+} cations of perovskite-type phase are partly carbonated as judging from the high CO_3^{2-}/La surface ratios (Table 3). The concentration of surface carbonates decreased slightly in $LaNi_{0.095}Rh_{0.05}O_3$ samples. On the other hand, Rh/La surface atomic ratios were higher than the nominal values. This fact seems to indicate the presence of a rhodium oxide phase, produced from Rh runoff from the perovskite-type structure during catalyst synthesis.

Atomic Ni/La and Rh/La ratios for used catalysts were also measured by EDX and compared to those of fresh samples (Table 4). Ni/La experimental ratios for samples obtained from sol–gel synthesis were comparable to nominal values. On the other hand, there was a decrease on the Ni/La ratios for co-precipitated catalysts. This difference could be associated to the fact that the samples prepared by co-precipitation generated smaller nickel particles (see Table 1). These smaller nickel particles are probably very active for methane dissociation and more prone to be covered by carbon deposits. In addition, since these nickel particles are small, they are more likely to undergo a sintering process. Both processes lead to a lower Ni/La ratio. Similar to what was observed for Ni/La ratios, the sample prepared by co-precipitation presented a Rh/La ratio after the reaction smaller than the nominal value, while for the catalyst obtained by sol–gel, the Rh/La ratio after the reaction was closer to the nominal value. The same hypothesis presented before could be used here.

TEM analysis of used $LaNi_{1-x}Rh_xO_3$ catalysts after 24 h on-stream is displayed in Fig. 8. All samples show spherical nickel particles. These images agree well with XRD data and indicate that metallic particles from the samples prepared by sol–gel undergo less sintering and are more dispersed, thus less prone to form carbonaceous deposits especially of amorphous type. As can be observed (Table 4), particle sizes of metallic Ni, derived from TEM images fall within the range 10–35 nm, depending on the synthesis method used to prepare the precursors. Not only nickel but also carbon deposits and a La-phase corresponding probably to a lanthanum dioxomonocarbonate and/or lanthanum hydroxide, were also observed. The carbonaceous deposits were found to be of nanotube-type with the metal particles located either at the end or within the carbon nanotube. In agreement with previous findings [27,40], metallic nickel particles favor formation of filamentous carbon deposits on the metallic nickel whose mechanism of formation demands sizes of at least 6 nm and carbon diffusion across the metal particle in accordance with our results (see Table 1).

3.5. Catalytic activity

Prior to reaction, the perovskite-type oxide precursors were activated in H_2 atmosphere to generate the active metal phase (Ni^0 or Ni^0–Rh^0) dispersed on La_2O_3. Then catalytic activity in the dry reforming reaction was measured as a function of the reaction temperature; results are shown in Fig. 9. All catalysts showed high activity for the dry reforming of methane. It is observed that at low reaction temperatures (400–500 °C), all samples presented similar activity, with the exception of the catalyst obtained from $LaNiO_3$-imp oxide, which had a lower methane conversion. At temperatures above 600–650 °C, this trend changed with $LaNiO_3$-imp and $LaNi_{0.95}Rh_{0.05}O_3$-cp being the most actives. In addition, activity of $LaNi_{0.95}Rh_{0.05}O_3$-sg catalysts markedly increased.

Stability tests were conducted for 24 h on-stream at 550 °C. Being far from thermodynamic constraints, results at this temperature allows comparison of catalysts performance. CH_4 and CO_2 conversion-reaction time profiles of all catalysts are displayed in Fig. 10. With the exception of the catalyst obtained from $LaNiO_3$-sg precursor which showed almost constant activity along the 24 h on-stream, a slight activation during reaction occurs for all catalysts. This activation period is the necessary time to fully reduce and stabilize the metal particles on the surface of the support. In fact, the samples prepared by co-precipitation, which are more crystalline as seen by XRD results, are probably more difficult to reduce, which could explain the longer activation periods in methane conversion observed for these samples (Fig. 10). In addition, the observed activation period for CO_2 conversion could also be related to formation of a $La_2O_2CO_3$ phase.

After 24 h on stream the trend of CH_4 conversion is as follows:

$LaNi_{0.95}Rh_{0.05}O_3$-sg > $LaNi_{0.95}Rh_{0.05}O_3$-cp > *LaNiO*$_3$-cp > $LaNiO_3$-imp > $LaNiO_3$-sg.

This indicates that partial substitution of Ni by Rh enhances CH_4 conversion and that $LaNiO_3$-cp is more active, although it requires longer activation time, than its $LaNiO_3$-sg counterpart.

CO_2 conversion profiles also exhibited a slight activation with time on-stream, with CO_2 conversions being somewhat higher than those of CH_4. For the two Rh-substituted solids, the CO_2 conversion-reaction time profiles are almost identical. In addition, the amount of CO_2 transformed by these two Rh-containing

Table 4
Atomic ratio and mean particle size of used catalysts determined by EDX and TEM analysis

Catalyst precursors	Atomic ratio calcined (theoretical)		Atomic ratio used catalysts (experimental)		Size distribution used catalysts (nm)
	Ni/La	Rh/La	Ni/La	Rh/La	
$LaNiO_3$-sg	1	–	0.93	–	8–19
$LaNiO_3$-cp	1	–	0.78	–	15–35
$LaNi_{0.95}Rh_{0.05}O_3$-sg	1	0.05	0.93	0.06	12–15
$LaNi_{0.95}Rh_{0.05}O_3$-cp	1	0.05	0.70	0.03	12–36

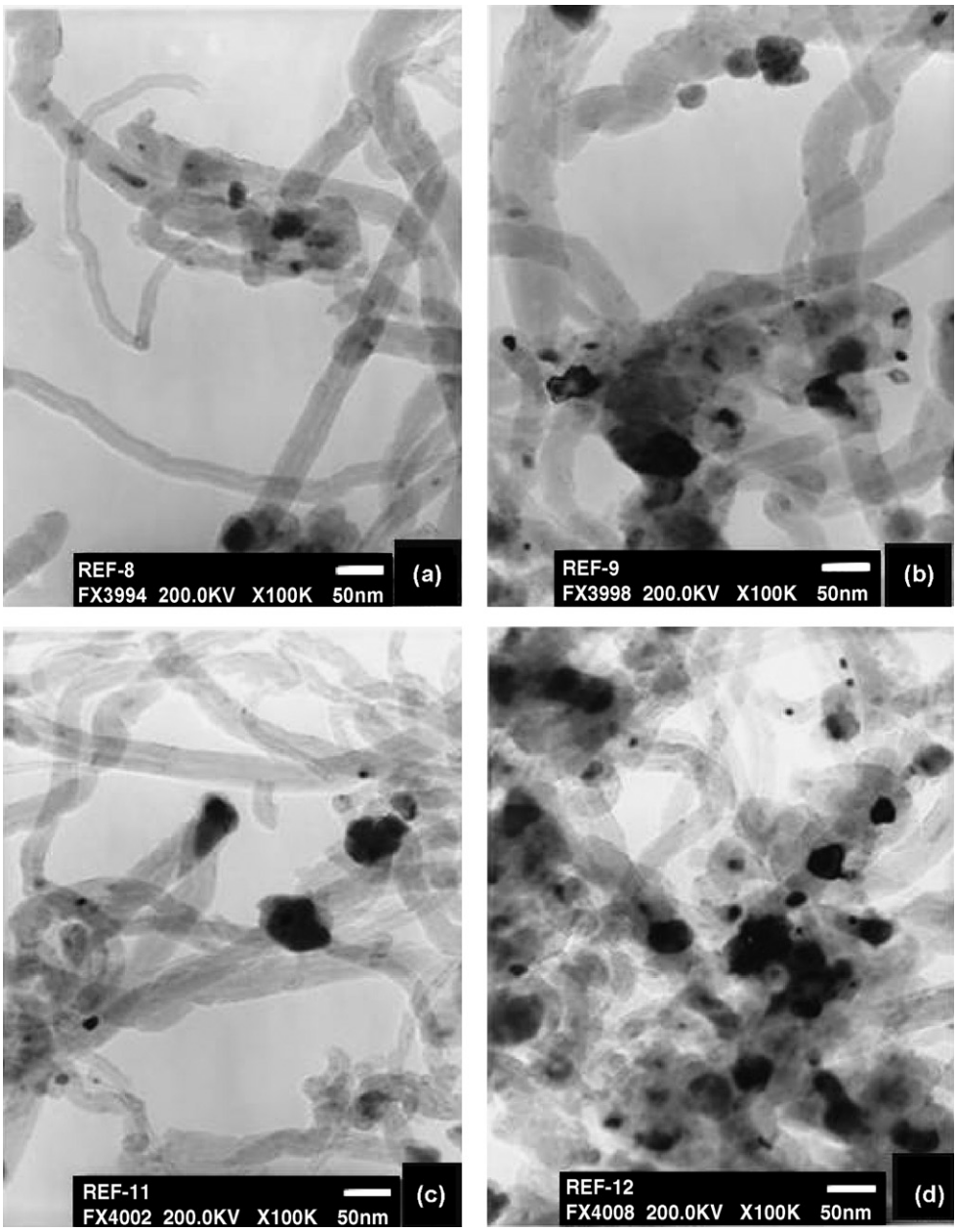

Fig. 8. TEM images of catalysts after 24 h on stream: (a) $LaNiO_3$-sg; (b) $LaNiO_3$-cp; (c) $LaNi_{0.95}Rh_{0.05}O_3$-sg; (d) $LaNi_{0.95}Rh_{0.05}O_3$-cp.

samples is higher than those observed for $LaNiO_3$-cp and $LaNiO_3$-sg samples. Again, longer reaction times were needed to reach catalyst steady state for CO_2 conversion on $LaNiO_3$-cp which was a little higher than that of the parent $LaNiO_3$-sg.

The higher CO_2 conversion obtained compared to that of CH_4 shown by all catalysts suggests that, in addition to the reforming reaction, the secondary reverse water–gas shift (RWGS) reaction takes place (Eq. (4)). As observed (Fig. 11), H_2/CO ratios are slightly lowers than 1 corroborating the occurrence of RWGS reaction by which some of the produced H_2 reacts with CO_2 to yield CO and H_2O. Evidence of the participation of the RWGS reaction comes also by the presence of water at the reactor outlet.

$$CO_2 + H_2 \rightarrow CO + H_2O \quad (4)$$

In agreement with other authors, the RWGS reaction (Eq. (4)) appears to be favored at low methane conversions [12,25]. In addition, there is probably another side reaction occurring: the catalytic decomposition of methane (CDM), which forms H_2 and carbon. Therefore, this reaction could explain the small differences observed when comparing CO_2 and CH_4 conversions, as well as, the H_2/CO ratios being not very far from unity.

It has been previously established that the rate of CO_2 dissociation on nickel particles is insignificant when compared to the rate of CDM [12]. In other words, CH_4 conversion being a function of CDM rate. On the other hand, CO_2 molecules strongly interact with La_2O_3 to form $La_2O_2CO_3$ type species. This phase reacts with carbon deposits on the surface of nickel particles, forming CO, which is then released to the gas phase. In addition, the RWGS also takes place, with CO_2 reacting with hydrogen on the surface to produce $CO + H_2O$. Therefore, CO_2 conversions are influenced by its interaction with $La_2O_2CO_3$ and by the rate of RWGS. In this study, the CO_2 conversion is favored for the catalysts that contain rhodium via RWGS. It is also interesting to point out

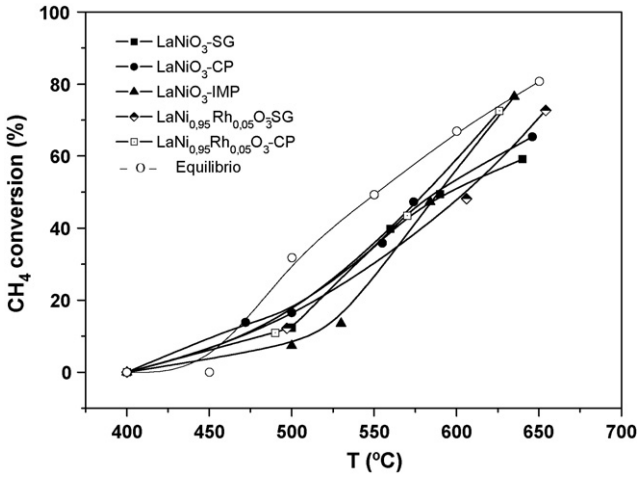

Fig. 9. CH_4 conversion as a function of temperature for catalysts derived from: $LaNiO_3$-sg, $LaNiO_3$-cp, $LaNi_{0.95}Rh_{0.05}O_3$-sg, and $LaNi_{0.95}Rh_{0.05}O_3$-cp precursors. Activation = 700 °C/2 h, $T_R = T_R$ = 400–600 °C, WHSV = 140 h^{-1}, and CH_4/CO_2 = 1.

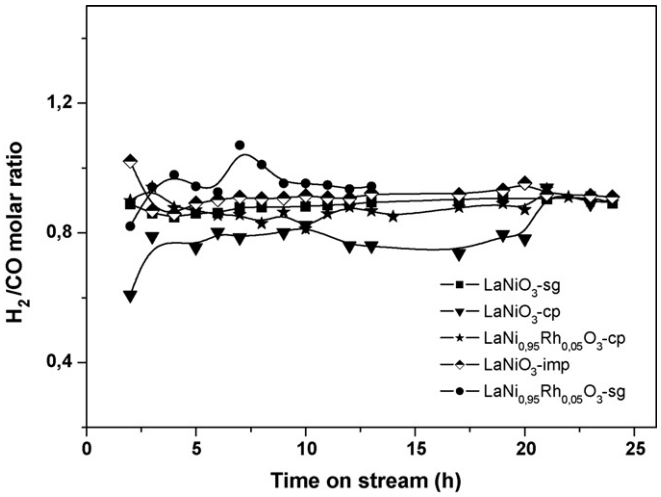

Fig. 11. H_2/CO ratio as a function of time on stream at 550 °C for catalysts derived from $LaNiO_3$-sg, $LaNiO_3$-cp, $LaNi_{0.95}Rh_{0.05}O_3$-sg, and $LaNi_{0.95}Rh_{0.05}O_3$-cp precursors. Activation = 700 °C/2 h, T_R = 550 °C, WHSV = 140 h^{-1}, and CH_4/CO_2 = 1.

that CO_2 conversions for $LaNiO_3$-imp sample is comparable to the values observed for rhodium containing samples. This is probably due to the fact that $LaNiO_3$-imp has more lanthanum oxide on the surface as observed by XRD results. This La_2O_3 may be promoting CO_2 conversions via formation of $La_2O_2CO_3$.

Catalysts derived from $LaNi_{0.95}Rh_{0.05}O_3$ precursors displayed slightly higher CH_4 and CO_2 conversions at catalyst steady state. This behavior could be explained by formation of highly dispersed Rh clusters which remain on the perovskite-type and/or La_2O_3 substrate during on-stream operation. In addition, TPR showed

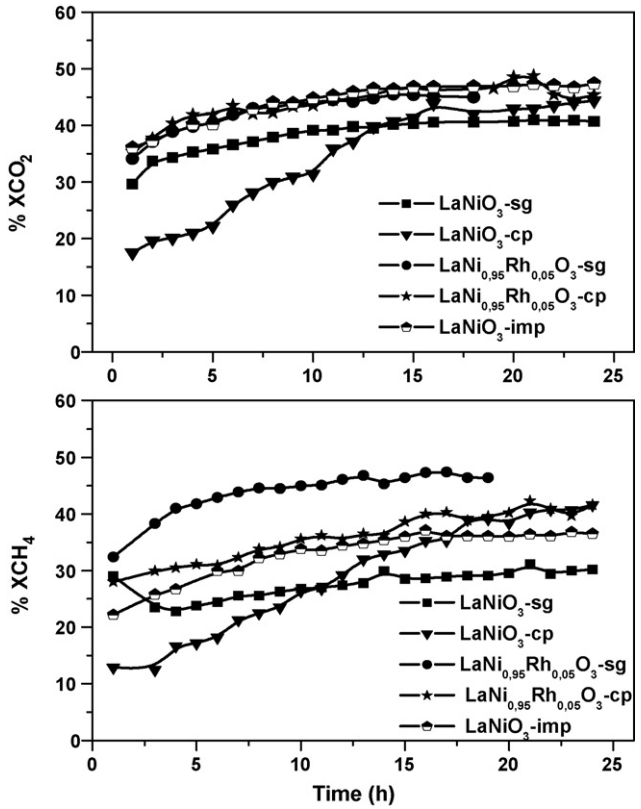

Fig. 10. CH_4 and CO_2 conversion as a function of time on stream at 550 °C for catalysts derived from $LaNiO_3$-sg, $LaNiO_3$-cp, $LaNi_{0.95}Rh_{0.05}O_3$-sg, and $LaNi_{0.95}Rh_{0.05}O_3$-cp precursors. Activation = 700 °C/2 h, T_R = 550 °C, WHSV = 140 h^{-1}, and CH_4/CO_2 = 1.

that the presence of Rh increases the reducibility of Ni cations from the perovskite-type oxides, producing a higher concentration of the active phase on the surface of the support.

In general, a relationship among specific surface area, particle size of reduced samples and catalytic behavior in the dry reforming reaction seems to exist. This is clearly illustrated by the higher CH_4 and CO_2 conversions observed for $LaNiO_3$-cp and $LaNiO_3$-imp samples which indeed exhibited the largest specific areas. In addition, XRD and TEM results showed that the samples obtained by co-precipitation are more prone to sintering during the reaction period, which in turn favors the formation of carbon deposits.

The catalyst obtained from activated $LaNiO_3$-sg precursor displayed good stability even though its specific surface area was lower than those obtained for the co-precipitated or impregnated samples. The observed stability of these Ni catalysts during 24 h on-stream indicates formation of small metal particles evenly distributed over the support. High stability may be also linked to the formation of $La_2O_2CO_3$ phase as detected by XRD and TEM analyses. Zhang et al. [41] pointed out that the carbon species formed on the Ni-sites are favorably removed by the oxygen species originating from $La_2O_2CO_3$ giving rise to active and stable performance due to the existence of synergetic sites consisting of Ni and La elements. Moreover, as it has been previously discussed [40–42] the Ni particle morphology and its size distribution influenced the origin, kinetics and reactivity of carbon deposition under reforming reactions conditions. In this case, nanotube type carbon was favored. The carbon nanotube which kept active the Ni particles extracted from the support growing to nanotube only produces deactivation of the catalysts after massive accumulation.

4. Conclusions

Highly homogeneous and crystalline solids were obtained by different synthesis methods. Characterization of the solids reveal the complete decomposition of perovskite-type structure after reduction with formation of metallic species such as Ni and Rh, and the presence of considerable amount of $La_2O_2CO_3$. The stability shown by these solids indicate that this phase highly contribute to catalyst resistance to deactivation.

Performance of the different synthesized precursors of catalysts could be related to metal particle size generated during the reduction pretreatment. It was observed that samples obtained by co-precipitation produce smaller metallic nickel particles, how-

ever, these particles tend to sinterized during on-stream operation; while the sol–gel synthesized precursors yielded metal crystallites that are thermally more stable. Influence of the synthesis procedure on the catalytic performance of the solids by formation of different lanthanum phases during reaction was observed.

The benefit of adding a small amount of rhodium to Ni-based perovskites ($LaNi_{0.95}Rh_{0.5}O_3$) was shown. The presence of rhodium not only modifies catalyst surface but it also improves catalytic performance by enhancing nickel reduction and dispersion as shown by TPR. The good catalytic performance shown by these solids in the dry reforming reaction is attributed to *in situ* formation under reaction conditions of highly dispersed metal particles (Ni, Rh/La-oxides) as a consequence of drastic structural changes suffered by the crystalline network of the perovskite-type precursors as revealed by *in situ* XRD and TEM analyses. The observed stability of the materials can be mainly attributed to formation of a $La_2O_2CO_3$ phase which enhances removal of carbonaceous deposits, and to the presence of filamentous carbon which do not directly deactivate the catalyst.

Acknowledgments

One of the authors (MER) gratefully acknowledges financial support for a doctoral fellowship (I3P-program) from the European Social Fund. Financial support from MEC, Spain (Project ENE2004-07345-C03-01/ALT) is also acknowledged.

References

[1] S. Teuner, Hydrocarbon Process 64 (1985) 106–107.
[2] L. Bedel, A.-C. Roger, J.-L. Rehspringer, Y. Zimmermann, A. Kiennemann, J. Catal. 235 (2005) 279–294.
[3] M.E. Dry, Catal. Today 71 (2002) 227–241.
[4] H.S. Bengaard, J.K. Nørskov, J.S. Sehested, B.S. Clausen, L.P. Nielsen, A.M. Molenbrock, J.R. Rostrup-Nielsen, J. Catal. 209 (2002) 365–384.
[5] J.S.H.Q. Perera, J.W. Couves, G. Sankar, J.M. Thomas, Catal. Lett. 11 (1991) 219–225.
[6] F. Solymosi, G. Kutsan, A. Erdohelyi, Catal. Lett. 11 (1991) 149–156.
[7] C. Batiot-Dupeyrat, G. Valderrama, A. Meneses, F. Martínez, J. Barrault, J.M. Tatibouet, Appl. Catal. A: Gen. 248 (2003) 143–151.
[8] M.R. Goldwasser, M.E. Rivas, E. Pietri, M.J. Pérez-Zurita, M.L. Cubeiro, L. Gengembre, L. Leclercq, G. Leclercq, Appl. Catal. A: Gen. 255 (2003) 45–57.
[9] A.J. Brungs, A.P.E. York, J.B. Claridge, C. Márquez-Álvarez, M.L.H. Green, Catal. Lett. 70 (2000) 117–122.
[10] J.B. Claridge, A.P.E. York, A.J. Brungs, C. Márquez-Álvarez, J. Sloan, S.C. Tsang, M.L.H. Green, J. Catal. 180 (1998) 85–100.
[11] T.C. Xiao, A. Hanif, A.P.E. York, Y. Nishizaka, M.L.H. Green, Phys. Chem. Chem. Phys. 4 (2002) 4549–4554.
[12] V.A. Tsipouriari, X.E. Verykios, Catal. Today 64 (2001) 83–90.
[13] M.C.J. Bradford, M.A. Vannice, J. Catal. 173 (1998) 157–171.
[14] Z.L. Zhang, X.E. Verykios, Appl. Catal. A 138 (1996) 109–133.
[15] J.H. Bitter, K. Seshan, J.A. Lercher, J. Catal. 176 (1998) 93–101.
[16] M. Bradford, M.A. Vannice, J. Catal. 183 (1999) 69–75.
[17] S. Tang, L. Ji, J. Lin, H.C. Zeng, K.L. Tan, K. Li, J. Catal. 194 (2000) 424–430.
[18] V.R. Choudary, B.S. Uphade, A.S. Mamman, Catal. Lett. 32 (1995) 387–390.
[19] S.M. Lima, J.M. Assaf, M.A. Peña, J.L.G. Fierro, Appl. Catal. A 331 (2006) 94–104.
[20] M.R. Goldwasser, M.E. Rivas, E. Pietri, M.J. Pérez-Zurita, M.L. Cubeiro, A. Griboval-Constant, G. Leclercq, J. Mol. Catal. A 228 (2005) 325–331.
[21] S. Ponce, M.A. Peña, J.L.G. Fierro, Appl. Catal. B 24 (2000) 193–205.
[22] A.K. Norman, M.A. Morris, J. Mater. Process. Technol. 92–93 (1999) 91–96.
[23] Pechini, M.P. US Patent 3,330,697 (1967)..
[24] F. Simonot, G. Gain, G. Maire, Appl. Catal. B 11 (1997) 167–179.
[25] G. Sierra, F. Mondragón, J. Barrault, J.M. Tatibouët, C. Batiot-Dupeyrat, Appl. Catal. A 311 (2006) 164–171.
[26] A. Slagtern, Y. Schuurman, C. Leclercq, X. Verykios, C. Mirodatos, J. Catal. 172 (1997) 118–126.
[27] J. Guo, H. Lou, Y. Zhu, X. Zheng, Mater. Lett. 57 (2003) 4450–4455.
[28] R. Tan, Y. Zhu, J. Feng, S. Ji, L. Cao, J. Alloys Comp. 337 (2002) 282–288.
[29] G. Valderrama, M.R. Goldwasser, C. Urbina, J.M. Tatibouët, J. Barrault, C. Batiot-Dupeyrat, F. Martínez, Catal. Today 107 (2005) 785–791.
[30] H.P. Klug, L.E. Alexander, X-ray Diffraction Procedures for Polycrystalline and Amorphous Materials, Wiley, London, 1962.
[31] J. Requies, M.A. Cabrero, V.L. Barrio, M.B. Guëmez, J.F. Cambra, P.L. Arias, F.J. Peréz-Alonso, M. Ojeda, M.A. Peña, J.L.G. Fierro, Appl. Catal. A 289 (2005) 214–223.
[32] Y. Mukainakano, Li. Baitao, S. Kado, T. Miyazagua, K. Okumura, T. Miyao, S. Naito, K. Kunimori, K. Tomishigue, Appl. Catal. A 318 (2007) 252–264.
[33] J.-H. Kim, D. Jin Suh, T.-J. Park, K.-L. Kimet, Appl. Catal. A 197 (2000) 191–200.
[34] J.S. Ledford, M. Houalla, A. Proctor, D.M. Hercules, J. Phys. Chem. 93 (1989) 6770–6777.
[35] M.A. Peña, J.L.G. Fierro, Chem. Rev. 101 (2001) 1981–2017.
[36] J.L.G. Fierro, Catal. Today 8 (1990) 153–174.
[37] H.J. Gysling, J.R. Monnier, G. Apai, J. Catal. 103 (1987) 407–418.
[38] R.M. García de la Cruz, H. Falcón, M.A. Peña, J.L.G. Fierro, Appl. Catal. B 33 (2001) 45–55.
[39] C.D. Wagner, L.E. Davis, M.V. Zeller, J.A. Taylor, R.H. Raymond, L.H. Gale, Surf. Interface Anal. 3 (1981) 211–225.
[40] B. Pawelec, S. Damyanova, K. Arishtirova, J.L. Fierro, G.L. Petrov, Appl. Catal. A 323 (2007) 188–201.
[41] W.D. Zhang, B.S. Liu, C. Zhu, Y.L. Tian, Appl. Catal. A 292 (2005) 138–143.
[42] M.A. Goula, A.A. Lemonidou, A.M. Efstathiou, J. Catal. 161 (1996) 626–640.